crystals

MDPI

Communication

Synchrotron Microbeam Diffraction Studies on the Alignment within 3D-Printed Smectic-A Liquid Crystal Elastomer Filaments during Extrusion

Marianne E. Prévôt [1], Senay Ustunel [1,2,†], Benjamin M. Yavitt [3,†,‡], Guillaume Freychet [3], Caitlyn R. Webb [1,4], Mikhail Zhernenkov [3], Elda Hegmann [1,2,4,5,6,*] and Ron Pindak [3,*]

1 Advanced Materials and Liquid Crystal Institute, Kent State University, Kent, OH 44242-001, USA; mprevot1@kent.edu (M.E.P.); sustunel@kent.edu (S.U.); cwebb14@kent.edu (C.R.W.)
2 Materials Science Graduate Program, Kent State University, Kent, OH 44242-001, USA
3 National Synchrotron Light Source-II, Brookhaven National Laboratory, Upton, NY 11973, USA; benjamin.yavitt@stonybrook.edu (B.M.Y.); gfreychet@bnl.gov (G.F.); zherne@bnl.gov (M.Z.)
4 Department of Biological Sciences, Kent State University, Kent, OH 44242-001, USA
5 Brain Health Research Institute, Kent State University, Kent, OH 44242-001, USA
6 Biomedical Sciences Program, Kent State University, Kent, OH 44242-001, USA
* Correspondence: ehegmann@kent.edu (E.H.); rpindak@bnl.gov (R.P.)
† Equal contribution to the manuscript.
‡ Now at Department of Chemistry, University of British Columbia, Vancouver, BC V6T 1Z1, Canada.

check for updates

Citation: Prévôt, M.E.; Ustunel, S.; Yavitt, B.M.; Freychet, G.; Webb, C.R.; Zhernenkov, M.; Hegmann, E.; Pindak, R. Synchrotron Microbeam Diffraction Studies on the Alignment within 3D-Printed Smectic-A Liquid Crystal Elastomer Filaments during Extrusion. *Crystals* **2021**, *11*, 523. https://doi.org/10.3390/cryst11050523

Academic Editor: Charles Rosenblatt

Received: 1 April 2021
Accepted: 4 May 2021
Published: 8 May 2021

Publisher's Note: MDPI stays neutral with regard to jurisdictional claims in published maps and institutional affiliations.

Copyright: © 2021 by the authors. Licensee MDPI, Basel, Switzerland. This article is an open access article distributed under the terms and conditions of the Creative Commons Attribution (CC BY) license (https://creativecommons.org/licenses/by/4.0/).

Abstract: 3D printing of novel and smart materials has received considerable attention due to its applications within biological and medical fields, mostly as they can be used to print complex architectures and particular designs. However, the internal structure during 3D printing can be problematic to resolve. We present here how time-resolved synchrotron microbeam Small-Angle X-ray Diffraction (μ-SAXD) allows us to elucidate the local orientational structure of a liquid crystal elastomer-based printed scaffold. Most reported 3D-printed liquid crystal elastomers are mainly nematic; here, we present a Smectic-A 3D-printed liquid crystal elastomer that has previously been reported to promote cell proliferation and alignment. The data obtained on the 3D-printed filaments will provide insights into the internal structure of the liquid crystal elastomer for the future fabrication of liquid crystal elastomers as responsive and anisotropic 3D cell scaffolds.

Keywords: liquid crystals; liquid crystal elastomers; 3D printing; anisotropy; advanced manufacturing; additive manufacturing; synchrotron X-ray microbeam; SAXD; smectic-A; orientational order

1. Introduction

Synchrotron X-ray microbeam diffraction has been widely used to correlate optical microscopy images with local X-ray structure. One of the earliest studies was done on beamline 4A at the Photon Factory to characterize the local layer structure across a broad wall in a surface-stabilized ferroelectric liquid crystal (FLC) [1]. Other X-ray microbeam liquid crystal (LC) studies include the time-resolved study of an FLC [2], elucidation of the structure of LC phases derived from bent-core molecules [3], a combined X-ray microbeam, polarized optical microscopy, a scanning electron microscopy study of the internal structure of periodic smectic-A (Sm-A) zig-zag defects from mesoscopic scale to molecular level [4], and the determination of orientational periodicities in the LC smectic-C* (Sm-C*) subphases by using an X-ray energy at the resonant edge of selenium-containing compounds [5]. One of the authors (RP) performed his first X-ray microbeam experiment with Professor Clark's group to correlate polarized optical microscopy images with local X-ray microbeam diffraction from short DNA oligomers [6]. This was a highly memorable project that was later highlighted in an engaging book [7]. In the current work, X-ray

microbeam diffraction is used to elucidate the evolving local structure as a liquid crystal elastomer (LCE) composite ink is three-dimensional (3D) printed.

Recently, new software and hardware advances in additive manufacturing (AM) or 3D printing, have been explored to pattern novel and smart materials with complex [8] and specific requirements increasing 3D printing applications into biological and medical fields [9,10]. Extrusion-based printing of semi-crystalline polymers is usually performed by the fused filament fabrication (FFF) technique, while the printing of pastes and structured fluids is done through continuous direct ink writing (DIW) [11,12]. Information about the structure formation during 3D printing is difficult to resolve, especially at the nanoscale. Thermal imaging has been combined with in situ small-angle X-ray scattering (SAXS) and wide-angle X-ray scattering (WAXS) to observe crystallization in thermoplastic polymers printed by FFF, where the local temperature was correlated to the degree of crystallinity [13,14]. Recent examples of coherent X-ray techniques have revealed unprecedented access to help in the understanding of real-time structural transitions that occur during the 3D printing of amorphous polymer composites and ceramics [15–17].

3D biological constructs require functional and structural architectures for their very particular applications, and in terms of their utility require specific (matching) mechanical properties, biocompatibility and, in most cases, biodegradability [18,19]. As part of the exclusive group of smart materials, liquid crystal elastomers (LCE) have been identified as materials capable of reversible actuation and have recently been studied as viscous inks formed from un-crosslinked liquid crystal (LC) oligomers for soft robotics [20,21]. The LCE actuation comes from the alignment of the liquid crystal mesogens, that have long been used as agents for thermal stability [22], sensors [23], or actuators [24,25] during phase transition or extrusion during the 3D printing process. However, LCEs have been studied in more detail for applications in the biological field as cell scaffolds. LCEs' orientational order, optical, and anisotropic elastic properties [26,27] make them suitable for biological application as they promote the development of the extracellular matrix (ECM) [13,26,28], cell attachment and proliferation [29,30], as well as promoters of cell orientation and maturation [31,32]. Very recently, LCEs have been shown to control the dynamics of bacteria [33,34]. Most likely, the growing interest in LCEs is because they can be used to create complex 3D architectures representative of organs or animal models [35,36], or function as long-term multi-responsive cell scaffolds [13,28,37]. Their applications can be expanded to anticancer drug screening, drug discovery, and other pharmaceutical applications [38,39] as new tools for preventative medicine.

There are two main strategies to synthesize LCEs: when mesogenic moieties are attached as part of the polymer backbone, they are termed main-chain LC elastomers [36,40], while if they are attached as a side-chain (pendant) to the backbone, they are termed side-chain LC elastomers [40]. Depending on the organization of the mesogenic moieties within the bulk, a formation of nematic, smectic, or cholesteric forms, among others, will be observed [41]. When the mesogenic pendant moieties are end-on side-chain elastomers, an LCE smectic phase could be favored, while side-on mesogenic pendant moieties or main-chain mesogenic moieties would more preferably form a nematic phase because they prefer the long-range positional order [42]. In any case, the orientation of the mesogenic moieties is transferred to the bulk of the LCE. The alignment of LCEs has been mainly studied in films as the result of an external stimuli [43,44] and very recently on filaments from nematic LCEs' inks [31,33]. We have previously reported a biocompatible and biodegradable side-chain Sm-A LCE-based ink for 3D printing as a 3D cell scaffold. The photocrosslinkable 3D polycaprolactone (PCL)-based LCEs have been shown to induce anisotropic cell behavior without any external stimulus applied [45,46]. In this study, we used a photosensitive Sm-A LCE as ink for 3D printing and studied its Sm-A organization (anisotropy) as it extruded at room temperature forming filaments in situ inside the beamline hutch. We also report here the synchrotron microbeam Small-Angle X-ray Diffraction (μ-SAXD) data revealing the alignment of the Sm-A LC within the printed filament during extrusion. This work

provides an entirely new platform to study the 3D printing of Sm-A LCE elastomers and evaluates the effect of extrusion using synchrotron x-ray microbeam diffraction.

2. Materials and Methods

All air-sensitive manipulations and synthetic steps were performed under nitrogen gas. ε-Caprolactone (ε-CL, purchased from Alfa Aesar) was dried over calcium hydride (from Sigma-Aldrich) and distilled under reduced pressure. *D*, *L*-Lactide was used as received (from Alfa Aesar). Dipentaerythritol, triethylamine, methacryloyl chloride, and Irgacure 819 (Bis (2,4,6-trimethylbenzoyl)-phenylphosphine oxide) were used as received (Sigma-Aldrich). Cholesterol (purchased from Sigma-Aldrich) was modified to cholesteryl 5-hexynoate by following previous work [47,48]. All solvents used for the synthesis and purification were EMD Millipore grade purified by a Pure-Solv solvent purification system (Innovative Technology Inc., Oldham, UK).

Amber syringe barrel, white polyethylene piston, end cap and blue dispense tip with an internal diameter of 0.41 mm (Nordson PN 7018272) were purchased from Nordson.

The print was obtained with our in-house 405 nm photosensitive LCE-based ink containing Irgacure 819 photoinitiator (Bis (2,4,6-trimethylbenzoyl)-phenylphosphine oxide). A curing of 75 seconds was applied in situ followed by 15 minutes ex situ post-curing. The UV system consisted of an Omnicure S1500 UV lamp (200 W Mercury lamp with a 320–500 nm filter) at 75% intensity and used a light guide placed at 13 cm from the sample in situ and 20 cm during ex situ post-curing. The print was made onto a 25 μm thick polyimide substrate (CAPLINQ PN PIT2A).

Scanning electron microscopy (SEM) was performed on samples which were gold-coated (700 Å) using a sputter coater (Hummer VI-A, Anatech Ltd., Springfield, VA, USA) at 10 mA DC for 3 min. Images were obtained using Quanta 450 FEG SEM under high vacuum. ^{1}H and ^{13}C NMR of copolymers and elastomers were recorded in $CDCl_3$ at room temperature on a Bruker DMX 400 MHz instrument and referenced internally to residual peaks at 7.26 (^{1}H).

Synchrotron μ-SAXD

Measurements were performed in transmission mode of the Soft Matter Interfaces beamline (12-ID SMI) at the National Synchrotron Light Source II (NSLS-II) [49]. Scattering patterns were measured at 16.1 keV with a beam size at the sample position of 2.5 μm × 25 μm (V × H) and recorded on a Pilatus 300 K−W detector, consisting of 0.172 mm square pixels in a 1475 × 195 array, mounted at a fixed distance of 0.275 m from the sample position. The 2D raw SAXS images were acquired in-air and converted into q-space, followed by a fixed background subtraction. Local variations in thickness, liquid crystal concentration, and morphology may have impacted the baseline after subtraction of a fixed background. Reduced images were visualized in Xi-CAM software and radially and azimuthally integrated using a custom Python code [49].

3. Results and Discussion

In situ μ-SAXD and 3D printing experiments were performed on a customized 3D printing platform mounted in-line with the X-ray beam in the sample chamber of the Soft Matter Interfaces (SMI) beamline at NSLS-II. The printer design was detailed by Wiegart et al. [15]. The entire printer was placed on the sample stage equipped with full x, y, z translation to position the printing process in-line with the X-ray beam. An on-axis and wide-view camera were used to assist in the alignment. An extrusion barrel filled with LCE-based ink was positioned on the printhead and horizontally/vertically moved to print the ink across the substrate on the print bed (see Figure 1). LCE filaments were extruded through a 22 GA straight-tip metal nozzle with an inner diameter of 410 μm during translation of the barrel at 1.5 mm/s along the print bed onto a polyimide substrate. The distance between the nozzle and the substrate was kept constant at 300 μm. Constant extrusion pressure of 25 psi was controlled by a Nordson Ultimus V dispenser.

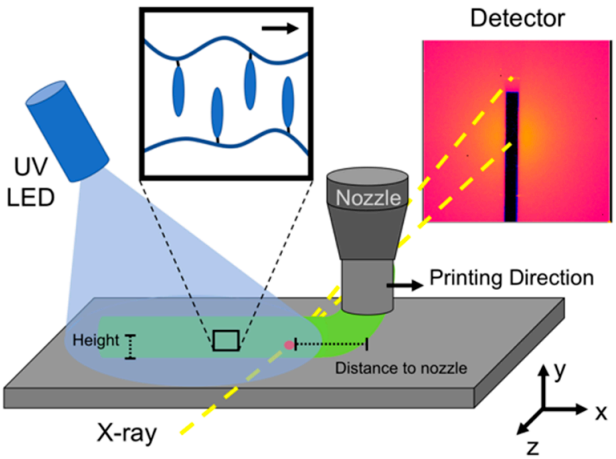

Figure 1. Schematic description of the 3D printing process coupled with in situ μ-SAXD, showing the position of the sample compared with the synchrotron X-ray beam.

The processing parameters were optimized for the ink viscosity to achieve smooth printability and reproducible filament structure, confirmed by Scanning Electron Microscopy (SEM) (Figure 2) performed on the printed filaments. The SEM images revealed that the filament experienced shape deformation at the substrate interface, forming a flat bottom after deposition due to relaxation, viscoelastic effects and wetting of the substrate. The flattening of the filament resulted in a reduction in the filament height in the solidified structure to about 240 μm compared to the 300 μm height expected from the settings of the nozzle height above the print bed. Overall, SEM images show a consistent shape and a homogeneous, void-free texture across the filament and cross-sectional areas.

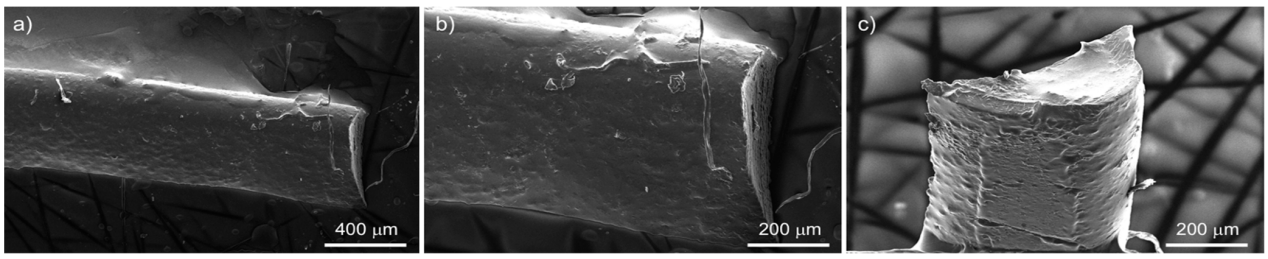

Figure 2. SEM images of 3D printed LCE filaments, (**a**) and (**b**) top view, and (**c**) the cross-section view.

The X-ray beam was oriented perpendicular to the printing direction. A UV curing system was focused onto the printing platform with an adjustable mounting arm at a fixed distance of ~13 cm from the intersection of the X-ray beam and the print bed (Figure 3). The illumination was oriented in the same direction as the horizontal printing. As a first experiment, the in situ printing and SAXS measurement protocol was as follows: printing began 5 mm away from the intersection of the X-ray beam and was horizontally translated towards the beam (Figure 3). The UV curing system was turned on as soon as the printing commenced to initiate crosslinking and was turned off after 75 s curing time. As the printed filament intersected the X-ray beam, a positional trigger was used to signal the 2D area detector to begin acquiring scattering patterns. The point at which the filament crossed the beam was designated as time = 0. The X-ray beam was located at a height of 150 μm above the print bed to characterize the structure formation in the approximate center of the filament. The microbeam sizing 2.5 × 25 μm (V × H) facilitated spatial scanning for a real-time structural analysis of the filament development.

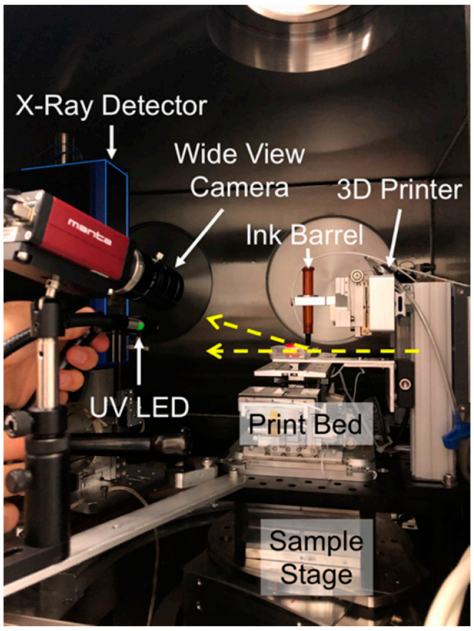

Figure 3. Optical image of the 3D printing setup coupled with in situ μ-SAXD inside the synchrotron hutch, the incident and scattered synchrotron X-ray beam path are represented with yellow arrows.

Thirty SAXS measurements were taken continuously at an exposure time of 1 s to resolve the structure as a function of distance from the advancing printing front. The structure could also be evaluated as a function of time after deposition with respect to time = 0. For each position, the radial and azimuthal μ-SAXD profiles were processed. The radial μ-SAXD profile exhibited two sharp scattering peaks at q_1 = 0.16 Å^{-1} and q_2 = 0.32 Å^{-1} characteristic of a Sm-A organization with interdigitated cholesterol moieties described in our previous work (see Figure 1 and Supplementary Information, SI Figure S1) [46–48,50]. μ-SAXD radial and azimuthal maps were extracted from the amplitude of the scattering peak and the amplitude of azimuthal integration, respectively, around q = 0.32 Å^{-1} (SI, Figure S1 and Figure 4, respectively). The Sm-A structure was found to be persistent over the filament length. Figure 4 reveals the alignment of the Sm-A layering with respect to the horizontal printing direction, which was designated as a 0 or 180° azimuthal angle on the scattering detector. The orientation of the Sm-A diffraction peaks (layer normal) appeared to be centered around 90° through the entirety of the printing process, indicating the long axis of the interdigitated moieties was aligned perpendicular to the printing direction. Therefore, the polymer chains would align along the flow direction to accommodate the LC side chain pendant configuration. The distribution around the preferential angle in the azimuthal map was centered on the intrinsic anisotropy associated with the extrusion process [26]. In comparison, a ring pattern was obtained in samples that were processed by film casting or particle leaching foam, suggesting the preferential alignment was induced by 3D printing [46,50,51]. Early in the filament development (time < 2.22 s), the orientation of the LCE layering was non-uniform, indicated by several individual streaks in intensity centered around 90°. The scattering pattern was reminiscent of powder-like diffraction due to discrete grains of aligned Sm-A that formed in the filament and pointed to a distribution of different directions (see SI, Video S1). The flow was likely chaotic at these early times as the LCE was deposited from the high shear and elongational stress present in the nozzle. After deposition and in the presence of the UV, the polymer chains began to crosslink, leading to an internal rearrangement, and a final structure was set in. After about 4 s (or a distance of 6 mm), the azimuthal intensity became more uniformly centered on 90°. Here, the LC layering orientation aligned to the preferred direction induced by the print direction. However, a few streaks were still identified, possibly due to the isolated grains that solidified in a partially offset direction during the progression of the UV curing (see

Figure S2). 3D printing is a complex non-equilibrium process: there can be high elongation and shear stress during extrusion from the nozzle, elongation in the 90° bend when exiting the nozzle, flow transverse to the print direction before LCE is crosslinked due to substrate wetting and relaxation, additional elongation stress resulting from printhead translation, and inhomogeneous UV curing across the filament. This complexity makes it difficult to predict how the SmA LCE will orient. In situ measurements of the orientational ordering are, therefore, required to optimize the processing parameters (pressure, speed, nozzle diameter, height above print bed, ink viscosity, cross-linker concentration, UV light intensity) to optimize the alignment. Our measurements demonstrate that we have identified a set of processing parameters that, after an initial disordered stage, provide a Sm-A LCE filament with the Sm-A layers aligned approximately parallel to the print direction within ±5 degrees.

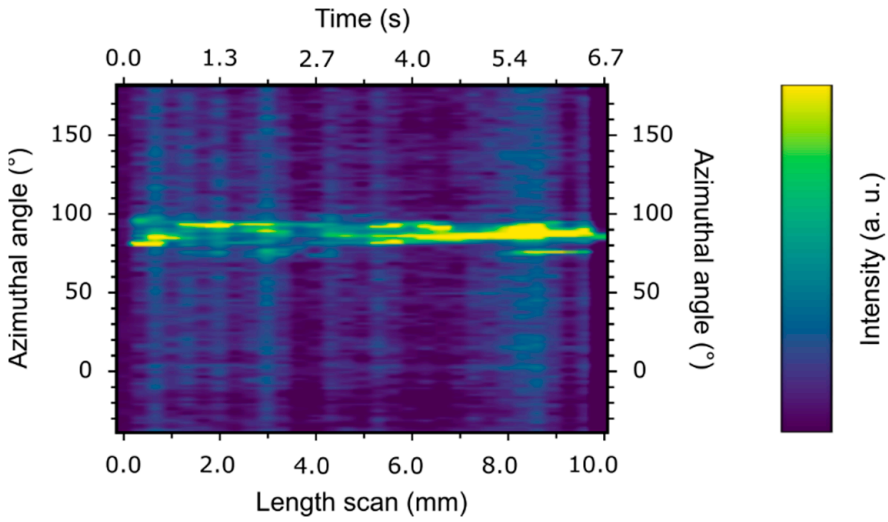

Figure 4. Real-time evolution of the μ-SAXD azimuthal profile of the Sm-A structure during the filament development: μ-SAXD azimuthal mapping of the filament taken with microbeam resolution as the printing occurred, both in respect to the distance from the advancing front (length scan) and time.

To expand the study of the orientation of the mesogenic moieties within the 3D structure, a second experiment consisting of a height scan was performed in the vertical direction once the filament was completely printed and fully cured. The microbeam precision allowed for resolution of the SmA layering alignment in the solidified 3D structure. The X-ray beam was positioned at 5 mm corresponding to the middle of the filament development. The base of the filament was calibrated with respect to the X-ray beam (h = 0 μm). The printer was translated at discrete steps of 9 μm in the vertical direction where at each point a SAXS image was taken, effectively scanning the sample as a function of height. Similar to the previous experiment, μ-SAXD radial and azimuthal maps were obtained, and the results are summarized in SI, Figure S3 and Figure 5, respectively, by the change in intensity in the azimuthal integration at q = 0.32 $Å^{-1}$ (integrated from q = 0.29 $Å^{-1}$ to q = 0.35 $Å^{-1}$) along the scanning height. Here, the Sm-A orientation evolved spatially throughout the filament (see Video S2 and Figure 5), likely influenced by the gradient in stress from the printing process as well as the UV light penetration through the thickness of the filament. At the substrate interface (h ~ 0 μm) the azimuthal angle intensity distribution was found to be narrow, suggesting strong alignment of the LCE layering. This region underwent a higher shear stress during printing compared to the bulk of the filament. As a consequence, the distribution of orientations increased, progressing in the bulk of the filament. The distribution can be quantitatively determined from 1D line cuts of the azimuthal intensity at various heights (see Figure S4). In the vicinity of the substrate interface, the layers were aligned parallel to the print direction,

with an approximate distribution of ±2°. As h increased, the distribution became wider to approximately ±3.5° at a height of h = 50 μm and a distribution of ±10° at h = 150 μm. Interestingly, besides the variation in the angular spread, the azimuthal angle distribution was maintained around 90°, indicating a persistence of the Sm-A layering alignment from the bottom to the top of the filament. At the top of the filament (h between 210 and 240 μm), the intensity decreased, possibly due to the curvature of the filament at the top of the interface. It is also likely that local heterogeneities in the concentration of liquid crystal (which was 20 wt.%) greatly impacted the scattering intensity, producing the apparent streaks in intensity observed in the height scan.

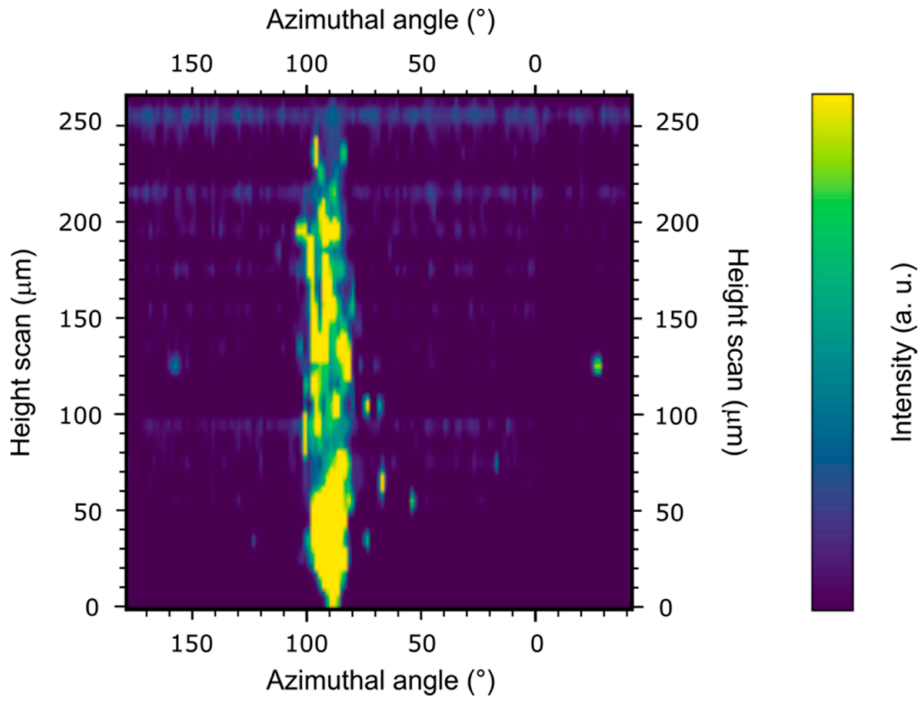

Figure 5. μ-SAXD azimuthal mapping of the Sm-A structure along the height of the filament taken with microbeam resolution after curing. 0 in height represents the interface between the substrate and the filament. The filament possessed a height of 240 μm.

In summary, after encountering initial external stimuli in situ during printing identified as compression in the barrel, shear stress during extrusion, and deformation at deposition pursued by relaxation and rearrangement post-deposition and during curing, the LCE layering alignment followed the preferred direction induced by the print direction. The specific alignment feature was then locked into the final structure. The preferential orientation of the Sm-A layering was particularly pronounced at the substrate interface. The preliminary investigation here demonstrated a technique merging time-resolved μ-SAXD and 3D printing towards the control of the degree and direction of LC layering orientation within the LCE-based printed scaffold. The μ-SAXD technique provided a 2D mapping of the Sm-A orientation with layer normal approximately perpendicular to the incident X-ray beam. We plan to conduct further ex situ studies rotating the sample with respect to the incident X-ray beam for a full 3D orientation map. In future work, we will explore the Sm-A layering alignment in rows of 3D-printed filaments intending to fabricate a fully active and responsive cell support structure into architectures to control cell directionality and anisotropy. This study will involve the integration of a multitude of cell types into this elastomer-ink, to help it become a bio-ink, and not only provide but also stimulate cell alignment. Our goal is to fabricate, among other tissues, complex vascular networks from the LCEs using 3D-printing containing cells.

Supplementary Materials: The data presented in this study are available within article and supplementary files at https://www.mdpi.com/article/10.3390/cryst11050523/s1, Figure S1: (a) 2D pattern at the substrate interface and (b) real-time radial μ-SAXD profile taken during the filament extrusion, Figure S2: 1D linecut representations of μ-SAXD azimuthal angle versus intensity at three different points of the length (L) scan (L= 6 mm in grey, L = 7.66 mm in blue, L = 9 mm in black), Figure S3: real-time radial μ-SAXD profile across the filament height, Figure S4: Representative 1D linecuts of azimuthal integration around q = 0.32 Å−1 versus intensity at different heights through the filament: at h = 5 μm (dark blue) close to the substrate interface, h = 50 μm (cyan), h = 100 μm (pink), and h = 150 μm (red); Video S1: PB077 height., and Video S1: PB077 during printing.

Author Contributions: S.U. and B.M.Y. contributed equally to this manuscript. E.H. and R.P. conceived the idea of the manuscript. M.E.P., and S.U., synthesized and characterized the LCEs prior to printing. C.R.W. helped collected early BNL data. M.E.P., S.U., B.M.Y., G.F., M.Z., R.P., and E.H. collected and analyzed all BNL data. M.Z., R.P., and E.H. directed all BNL experiments. M.E.P., B.M.Y., E.H. and R.P. prepared the manuscript draft with contributions from all authors. E.H. wrote all beamline proposals. R.P., and E.H. directed the research and finalized the manuscript with contributions of all authors. All authors have read and agreed to the published version of the manuscript.

Funding: This research used the Soft Matter Interfaces (SMI, 12-ID) of the National Synchrotron Light Source II (NSLS-II), a U.S. Department of Energy (DOE) Office of Science User Facility operated for the DOE Office of Science by Brookhaven National Laboratory (BNL) under Contract No. DE-SC0012704.

Data Availability Statement: The data presented in this study are available within article and supplementary files.

Acknowledgments: The authors want to thank the Liquid Crystal Characterization Facility at the Advanced Materials and Liquid Crystal Institute (AMLCI) where the SEM data was acquired. Authors also want to thank Lutz Wiegart for his help and expertise on the integration of the 3D printing platforms with synchrotron X-ray beamlines at BNL.

Conflicts of Interest: The authors have no conflict of interest to declare.

References

1. Iida, A.; Noma, T.; Miyata, H.; Mirano, K. Micro x-ray diffraction technique for analysis of the local layer structure in the ferroelectric liquid crystal. *Rev. Sci. Instrum.* **1995**, *66*, 1373–1375. [CrossRef]
2. Takahashi, Y.; Iida, A.; Takanishi, Y.; Ogasawara, T.; Ishikawa, K.; Takezoe, H. Dynamic behaviour of the local layer structure of antiferroelectric liquid crystals under a high electric field measured by time-resolved synchrotron x-ray microbeam diffraction. *Jpn. J. Appl. Phys.* **2001**, *40*, 3294–3300. [CrossRef]
3. Kang, S.; Tokita, M.; Takanishi, Y.; Takezoe, H.; Watanabe, J. Structure of a B6-like phase formed from bent-core liquid crystals determined by microbeam x-ray diffraction. *Phys. Rev. E* **2007**, *76*, 042701. [CrossRef]
4. Yoon, D.; Yoon, J.; Kim, Y.H.; Choi, M.C.; Kim, J.; Sakata, O.; Kimura, S.; Kim, M.W.; Smalyukh, I.I.; Clark, N.A.; et al. Liquid-crystal periodic zigzags from geometrical and surface-anchoring-induced confinement: Origin and internal structure from mesoscopic scale to molecular level. *Phys. Rev. E* **2010**, *82*, 041705. [CrossRef]
5. Feng, Z.; Perera, A.D.L.C.; Fukuda, A.; Vij, J.K.; Ishikawa, K.; Iida, A.; Takanishi, Y. Definite existence of subphases with eight- and ten-layer unit cells as studied by complementary methods, electric-field-induced birefringence and microbeam resonant x-ray scattering. *Phys. Rev. E* **2017**, *96*, 012701. [CrossRef]
6. Nakata, M.; Zanchetta, G.; Chapman, B.D.; Jones, C.D.; Cross, J.O.; Pindak, R.; Bellini, T.; Clark, N.A. End-to-end stacking and liquid crystal condensation of 6–to-20–base pair DNA duplexes. *Science* **2007**, *318*, 1276–1279. [CrossRef]
7. Yevdokimov, Y.M.; Sonin, A.S. DNA nanoscience: From prebiotic origins to emerging nanotechnology, by Kenneth Douglas, Boca Raton, CRC Press, 2016, 424 p. *Liq. Cryst. Today* **2016**, *25*, 82–84. [CrossRef]
8. Tran, V.; Wen, X. Rapid prototyping technologies for tissue regeneration. In *Rapid Prototyping of Biomaterials—Principles and Applications*; Narayan, R., Ed.; Woodhead Publishing: Cambridge, UK, 2014; pp. 97–155.
9. Lee, J.-Y.; An, J.; Chua, C.K. Fundamentals and applications of 3D printing for novel materials. *Appl. Mater. Today* **2017**, *7*, 120–133. [CrossRef]
10. Xu, T.; Rodriguez-Devora, J.I.; Reyna-Soriano, D.; Mohammod, B.; Zhu, L.; Wang, K.; Yuan, Y. Bioprinting for constructing microvascular systems for organs. In *Rapid Prototyping of Biomaterials—Principles and Applications*; Narayan, R., Ed.; Woodhead Publishing: Cambridge, UK, 2014; pp. 201–220.
11. Truby, R.L.; Lewis, J.A. Printing Soft Matter in Three Dimensions. *Nature* **2016**, *540*, 371–378. [CrossRef]
12. Mackay, M.E. The Importance of Rheological Behavior in the Additive Manufacturing Technique Material Extrusion. *J. Rheol.* **2018**, *62*, 1549–1561. [CrossRef]

13. Shmueli, Y.; Jiang, J.; Zhou, Y.; Xue, Y.; Chang, C.; Yuan, G.; Satija, S.K.; Lee, S.; Nam, C.; Kim, T.; et al. Simultaneous in Situ X-ray Scattering and Infrared Imaging of Polymer Extrusion in Additive Manufacturing. *ACS Appl. Polym. Mater.* **2019**, *1*, 1559–1567. [CrossRef]
14. Nogales, A.; Gutiérrez-Fernández, E.; García-Gutiérrez, M.-C.; Ezquerra, T.A.; Rebollar, E.; Šics, I.; Malfois, M.; Gaidukovs, S.; Gēcis, E.; Celms, K.; et al. Structure Development in Polymers during Fused Filament Fabrication (FFF): An in Situ Small- and Wide-Angle X-ray Scattering Study Using Synchrotron Radiation. *Macromolecules* **2019**, *52*, 9715–9723. [CrossRef]
15. Wiegart, L.; Doerk, G.S.; Fukuto, M.; Lee, S.; Li, R.; Marom, G.; Noack, M.M.; Osuji, C.O.; Rafailovich, M.H.; Sethian, J.A.; et al. Instrumentation for In Situ/Operando X-Ray Scattering Studies of Polymer Additive Manufacturing Processes. *Synchrotron Radiat. News* **2019**, *32*, 20–27. [CrossRef]
16. Yavitt, B.M.; Wiegart, L.; Salatto, D.; Huang, Z.; Endoh, M.K.; Poeller, S.; Petrash, S.; Koga, T. Structural Dynamics in UV Curable Resins Resolved by In Situ 3D Printing X-ray Photon Correlation Spectroscopy. *ACS Appl. Polym. Mater.* **2020**, *2*, 4096–4108. [CrossRef]
17. Torres Arango, M.A.; Zhang, Y.; Li, R.; Doerk, G.; Fluerasu, A.; Wiegart, L. In-Operando Study of Shape Retention and Microstructure Development in a Hydrolyzing Sol−Gel Ink during 3D-Printing. *ACS Appl. Mater. Interfaces* **2020**, *12*, 51044–51056. [CrossRef]
18. Bartolo, P.; Domingos, M.; Gloria, A.; Ciurana, J. BioCell Printing: Integrated Automated Assembly System for Tissue Engineering Constructs. *CIRP Annals* **2011**, *60*, 271–274. [CrossRef]
19. Prévôt, M.E.; Ustunel, S.; Hegmann, E. Liquid Crystal Elastomers—A Path to Biocompatible and Biodegradable 3D-LCE Scaffolds for Tissue Regeneration. *Materials* **2018**, *11*, 377. [CrossRef]
20. Wang, Z.; Wang, Z.; Zheng, Y.; He, Q.; Wang, Y.; Cai, S. Three-dimensional printing of functionally graded liquid crystal elastomer. *Sci. Adv.* **2020**, *6*, eabc0034. [CrossRef]
21. Ambulo, C.; Burroughs, J.J.; Boothby, J.M.; Kim, H.; Shankar, M.R.; Ware, T.H. Four-dimensional Printing of Liquid Crystal Elastomers. *ACS Appl. Mater. Interfaces* **2017**, *9*, 37332. [CrossRef]
22. Jang, K.-S.; Johnson, C.J.; Hegmann, T.; Hegmann, E.; Korley, L.T.J. Biphenyl-based liquid crystals for elevated temperature processing with polymers. *Liq. Cryst.* **2014**, *41*, 1473–1482. [CrossRef]
23. Prévôt, M.E.; Nemati, A.; Cull, T.R.; Hegmann, E.; Hegmann, T. A zero-power, ppt-to ppm-level toxic gas and vapor sensor with image, text, and analytical capabilities. *Adv. Mater. Technol.* **2020**, *5*, 2000058. [CrossRef]
24. Van Oosten, C.L.; Bastiaansen, C.W.M.; Broer, D.J. Printed artificial cilia from liquid-crystal network actuators modularly driven by light. *Nat. Mater.* **2009**, *8*, 677–682. [CrossRef]
25. Kularatne, R.S.; Kim, H.; Boothby, J.M.; Ware, T.H. Liquid Crystal Elastomer Actuators: Synthesis, Alignment, and Applications. *J. Polym. Sci. Part B Polym. Phys.* **2017**, *55*, 395–411. [CrossRef]
26. Ohm, C.; Brehmer, M.; Zentel, R. Applications of Liquid Crystalline Elastomers. In *Liquid Crystal Elastomers: Materials and Applications. Advances in Polymer Science*; De Jeu, W., Ed.; Springer: Berlin/Heidelberg, Germany, 2012; Volume 250. [CrossRef]
27. Prévôt, M.E.; Bergquist, L.E.; Sharma, A.; Mori, T.; Gao, Y.; Bera, T.; Zhu, C.; Leslie, M.T.; Cukelj, R.; Korley, L.T.J.; et al. New developments in 3D liquid crystal elastomers scaffolds for tissue engineering: From physical template to responsive substrate. In Proceedings of the SPIE Organic Photonics + Electronics, San Diego, CA, USA, 6–10 August 2017; Volume 103610T, pp. 1–11. [CrossRef]
28. Ustunel, S.; Prévôt, M.E.; Clements, R.J.; Hegmann, E. Cradle-to-Cradle: Designing Biomaterials to Fit as Truly Biomimetic Cell Scaffolds—A Review. *Liq. Cryst. Today* **2020**, *29*, 40. [CrossRef]
29. Martella, D.; Pattelli, L.; Matassini, C.; Ridi, F.; Bonini, M.; Paoli, P.; Baglioni, P.; Wiersma, D.; Parmeggiani, C. Liquid crystal induced myoblast alignment. *Adv. Healthc. Mater.* **2019**, *8*, 1801489. [CrossRef] [PubMed]
30. Babakhanova, G.; Krieger, J.; Li, B.-X.; Turiv, T.; Kim, M.-H.; Lavrentovich, O.D. Cell alignment by smectic liquid crystal elastomer coatings with nanogrooves. *J. Biomed. Mater. Res. Part A* **2020**, *108*, 1223–1230. [CrossRef] [PubMed]
31. Lockwood, N.A.; Mohr, J.C.; Ji, L.; Murphy, C.J.; Palecek, S.P.; de Pablo, J.J.; Abbott, N.L. Thermotropic liquid crystals as substrates for imaging the reorganization of matrigel by human embryonic stem cells. *Adv. Funct. Mater.* **2006**, *16*, 618–624. [CrossRef]
32. Prévôt, M.E.; Ustunel, S.; Bergquist, L.E.; Cukelj, R.; Gao, Y.; Mori, T.; Pauline, L.; Clements, R.J.; Hegmann, E. Synthesis of Biocompatible Liquid Crystal Elastomer Foams as Cell Scaffolds for 3D Spatial Cell Cultures. *J. Vis. Exp.* **2017**, *122*, e55452. [CrossRef]
33. Dhakal, N.P.; Jiang, J.; Guo, Y.; Peng, C. Self-Assembly of Aqueous Soft Matter Patterned by Liquid-Crystal Polymer Networks for Controlling the Dynamics of Bacteria. *ACS Appl. Mater. Interfaces* **2020**, *12*, 13680–13685. [CrossRef]
34. Turiv, T.; Koizumi, R.; Thijssen, K.; Genkin, M.M.; Yu, H.; Peng, C.; Wei, Q.-H.; Yeomans, J.M.; Aranson, I.S.; Doostmohammadi, A.; et al. Polar jets of swimming bacteria condensed by a patterned liquid crystal. *Nat. Phys.* **2020**, *16*, 481–487. [CrossRef]
35. Haycock, J.W. *3D Cell Culture: A Review of Current Approaches and Techniques. Methods in Molecular Biology 3D Cell Culture*; Humana Press: Totowa, NJ, USA, 2010; pp. 1–15. [CrossRef]
36. Liu, X.H.; Jin, X.B.; Ma, P.X. Nanofibrous hollow microspheres self-assembled from star-shaped polymers as injectable cell carriers for knee repair. *Nat. Mater.* **2011**, *10*, 398–406. [CrossRef]
37. Langer, R.; Vacanti, J.P. Tissue Engineering. *Science* **1993**, *260*, 920–926. [CrossRef] [PubMed]
38. Ravi, M.; Paramesh, V.; Kaviya, S.R.; Anuradha, E.; Paul, S.F.D. 3D Cell Culture Systems: Advantages and Applications. *J. Cell. Physiol.* **2015**, *230*, 16–26. [CrossRef] [PubMed]

39. Massa, S.; Sakr, M.A.; Seo, J.; Bandaru, P.; Arneri, A.; Bersini, S.; Zare-Eelanjegh, E.; Jalilian, E.; Cha, B.-H.; Antona, S.; et al. Bioprinted 3D vascularized tissue model for drug toxicity analysis. *Biomicrofluidics* **2017**, *11*, 044109. [CrossRef]
40. Degennes, P.G. One type of nematic polymers. *Comptes Rendus Hebd. Seances Acad. Sci. Ser. B* **1975**, *281*, 101–103.
41. Schneider, A.; Muller, S.; Finkelmann, H. Lyotropic mesomorphism of AB block copolymers in nematic solvents. *Macromol. Chem. Phys.* **2000**, *201*, 184–191. [CrossRef]
42. Broemmel, F.; Kramer, D.; Finkelmann, H. Preparation of liquid crystalline elastomers. In *Liquid Crystal Elastomers: Materials and Applications*; De Jeu, W.H., Ed.; Springer: Berlin/Heidelberg, Germany, 2012; Volume 250, pp. 1–48. [CrossRef]
43. Yakacki, C.M.; Saed, M.; Nair, D.P.; Gong, T.; Reed, S.M.; Bowman, C.N. Tailorable and programmable liquid-crystalline elastomers using a two-stage thiol–acrylate reaction. *RSC Adv.* **2015**, *5*, 18997–19001. [CrossRef]
44. He, Q.; Wang, Z.; Wang, Y.; Minori, A.; Tolley, M.T.; Cai, S. Electrically controlled liquid crystal elastomer–based soft tubular actuator with multimodal actuation. *Sci. Adv.* **2019**, *5*, eaax5746. [CrossRef]
45. Kotikian, A.; Truby, R.L.; Boley, J.W.; White, T.J.; Lewis, J.A. 3D Printing of Liquid Crystal Elastomeric Actuators with Spatially Programed Nematic Order. *Adv. Mater.* **2018**, *30*, 1706164. [CrossRef] [PubMed]
46. Sharma, A.; Mori, T.; Mahnen, C.J.; Everson, H.R.; Leslie, M.T.; Nielsen, A.D.; Lussier, L.; Zhu, C.; Malcuit, C.; Hegmann, T.; et al. Effects of structural variations on the cellular response and mechanical properties of biocompatible, biodegradable, and porous smectic liquid crystal elastomers. *Macromol. Biosci.* **2017**, *17*, 1600278. [CrossRef]
47. Prévôt, M.E.; Ustunel, S.; Freychet, G.; Webb, C.R.; Zhernenkov, M.; Pindak, R.; Clements, R.J.; Hegmann, E. Physical models from physical templates using biocompatible liquid crystal elastomers as new morphologically programmable inks for 3D printing. *J. Appl. Phys.* **2021**. in peer review.
48. Sharma, A.; Neshat, A.; Mahnen, C.J.; Nielsen, A.d.; Snyder, J.; Stankovich, T.L.; Daum, B.G.; LaSpina, E.M.; Beltrano, G.; Gao, Y.; et al. Biocompatible, Biodegradable and Porous Liquid Crystal Elastomer Scaffolds for Spatial Cell Cultures. *Macromol. Biosci.* **2015**, *15*, 200–214. [CrossRef] [PubMed]
49. Zhernenkov, M.; Canestrari, N.; Chubar, O.; DiMasi, E. Soft matter interfaces beamline at NSLS-II: Geometrical ray-tracing vs. wavefront propagation simulations. In Proceedings of the SPIE Optical Engineering + Applications 2014, San Diego, CA, USA, 18–21 August 2014; Volume 9209, p. 92090G. [CrossRef]
50. Prévôt, M.E.; Andro, H.; Alexander, S.L.M.; Ustunel, S.; Zhu, C.; Nikolov, Z.; Rafferty, S.T.; Brannum, M.T.; Kinsel, B.; Korley, L.T.J.; et al. Liquid crystal elastomer foams with elastic properties specifically engineered as biodegradable brain tissue scaffolds. *Soft Matter* **2018**, *14*, 354–360. [CrossRef]
51. Pandolfi, R.J.; Allan, D.B.; Arenholz, E.; Barroso-Luque, L.; Campbell, S.I.; Caswell, T.A.; Blair, A.; De Carlo, F.; Fackler, S.; Fournier, A.P.; et al. Xi-cam: A versatile interface for data visualization and analysis. *J. Synchrotron Radiat.* **2018**, *25*, 1261–1270. [CrossRef] [PubMed]